

X-ray Spectroscopic Fingerprints of Reactive Oxygen Sites at the MoO₃(010) Surface

**M. Cavalleri^{1*}, K. Hermann^{1*}, S. Guimond², Y. Romanyshyn², H. Kuhlenbeck²,
and H.-J. Freund²**

¹ Theory Department, Fritz-Haber-Institut der Max-Planck-Gesellschaft, Faradayweg 4-6, 14195 Berlin, Germany

² Department of Chemical Physics, Fritz-Haber-Institut der Max-Planck-Gesellschaft, Faradayweg 4-6, 14195 Berlin, Germany

The identification of oxygen sites at metal oxide surfaces and the characterization of their properties is of great importance for an understanding of the catalytic activity of such materials and, thus, for a rational design of efficient and selective catalysts. In the case of the clean MoO₃(010) surface we show that an unambiguous discrimination of the different reactive oxygen sites can be obtained by angle-resolved Near-Edge X-Ray Absorption Fine Structure (NEXAFS) combined with Density-Functional-Theory (DFT) based spectrum analyses for different photon polarization directions. In particular, we are able to unequivocally discriminate the characteristic spectral signatures of singly coordinated molybdenyl oxygen covering the topmost molybdenum layers from those of other oxygen centers that have very similar local environment and only differ by their spatial orientation in the crystal. Theoretical predictions are also successfully used to identify and interpret characteristic features in the NEXAFS spectra that arise from specific vacancy sites present at oxygen deficient surfaces.

Keywords: Molybdenum oxide, MoO₃, x-ray absorption, density functional theory

* Corresponding authors: cavall@fhi-berlin.mpg.de (M.Cavalleri), hermann@fhi-berlin.mpg.de (K.Hermann)

1. Introduction

Transition metal oxides form a fascinating class of materials with extremely interesting structural, electronic, and magnetic behavior, as for example high temperature superconductivity or exciting optical properties [1]. From a chemical viewpoint they play a fundamental role in heterogeneous catalysis of important chemicals, both in gas and liquid phase, as well as in acid-base and redox reaction processes of industrial interest [2]. In particular, molybdenum oxides are known to activate C-H bonds of alkanes, including methane, and catalyzing their selective partial oxidation, a process that otherwise requires extremely high temperatures. In mixed oxides, molybdenum (mainly with vanadium as the other basic catalyst component) is found to be reactive in other important reactions of interest to the chemical industry such as the dehydrogenation of propane to propene [3].

It has been shown, however, that the chemical complexity of mixed oxides is not necessarily required for catalytic efficiency since molybdenum oxide itself exhibits adequate structural complexity. In fact it has been suggested that the rich and diverse chemistry and high catalytic performance of molybdenum oxides lies in their ability to assume very different metal oxidation states, ranging from +4 to +6, and the variability of the oxygen coordination geometry [1, 4]. The latter includes tetrahedra, octahedra, pentagonal bipyramids, and square pyramids of molybdenum oxide, often coexisting in a plethora of structural arrangements where different local Mo_xO_y units share corners, edges, and faces. At molybdenum oxide surfaces the differently coordinated oxygen centers can participate in catalytic reactions either as reactive sites or, in the case of oxidation processes, can be directly involved as reaction components. Here different oxygen species are expected to react differently according to their specific binding environment [5]. Therefore, an analysis of the behavior and involvement of each oxygen species in particular reaction steps is essential for a detailed understanding of catalytic processes and, thus, for a rational design of more efficient and selective catalysts.

Corresponding analyses require an identification of differently coordinated oxygen species including their binding geometry. This identification can be rather difficult since corresponding experimental differences between the species are sometimes too subtle to enable discrimination. As an example, we mention results of 1s core ionization potentials of differently (1- to 3-fold) coordinated oxygen at the $\text{V}_2\text{O}_5(010)$ surface which differ by less than 0.5 eV from calculations [6] and, therefore, cannot be resolved in X-ray photoelectron

spectroscopy experiments. In addition, ultraviolet photoemission spectroscopy does not provide unique experimental discrimination between differently coordinated oxygen without the aid of theoretical density-of-states studies [7]. However, core excitation spectroscopy combining core information with that of local binding near the excitation atom can provide a rather reliable basis to discriminate between atoms in different coordination environments and analyze their binding properties. This has been shown successfully for free and adsorbed molecules [8-10], for surfaces [11, 12], and for bulk and interfacial systems [13-17] where theoretical Density-Functional Theory (DFT) studies of corresponding excitation spectra in comparison with (angle-resolved) Near-Edge X-ray Absorption Fine Structure (NEXAFS) measurements can yield very detailed information on a local atomic level.

In the present work we examine differently coordinated oxygen at the (010) surface of a MoO_3 single crystal. This substrate provides an excellent initial model for molybdenum oxide based catalysts since it offers a well-defined crystal structure while retaining structural complexity and variability of oxygen centers [4]. From theoretical DFT studies on appropriately chosen $\text{MoO}_3(010)$ surface clusters core excitation spectra are evaluated and compared with experimental angle-resolved NEXAFS spectra on clean $\text{MoO}_3(010)$ surfaces. The results demonstrate clearly that differently coordinated oxygen can be discriminated by this type of spectroscopy. In addition, we report preliminary theoretical results from DFT cluster studies on oxygen vacancies at the $\text{MoO}_3(010)$ surface. These vacancies are believed to determine the activity and selectivity of catalytic reactions at the metal oxide surface which is of great scientific and technological interest. As an example, reduced metal centers near oxygen vacancies are found to increase the activity of molybdenum oxide with respect to methane oxidation [18-20]. Our studies suggest that O 1s NEXAFS spectra taken near vacancies of deficient $\text{MoO}_3(010)$ differ substantially in their photon angle dependence from those of oxygen at the clean surface. They may, therefore, be used to identify oxygen vacancies in the experiment.

2. Computational Details

Bulk MoO_3 forms an orthorhombic crystal lattice with a layer structure of weakly binding bilayers parallel to (010) netplanes (reflecting the preferred cleavage planes of the crystal), see Fig. 1a. Each bilayer consists of two interleaved planes of distorted MoO_6 octahedra sharing a corner while octahedra from adjacent planes share edges [4, 21]. The (010) surface exposes three differently coordinated oxygen atoms, see Fig 1a, b. The terminal molybdenyl oxygen species, O(1), is connected to one molybdenum atom by a bond directed almost perpendicular to the surface plane. Bridging oxygen O(2) is coordinated asymmetrically to two Mo atoms with bond direction along the (100) direction while O(3) is coordinated symmetrically to two metal centers in the surface plane and, with longer distance, to one molybdenum in the underlaying plane of the bilayer. Table 1 lists typical interatomic distances at the $\text{MoO}_3(010)$ surface.

The molybdenum oxide surface is modeled by clusters of finite size reflecting the bulk terminated geometry and containing at least the complete first coordination shell of each oxygen center to be considered in the core excitation calculations. Previous theoretical studies and extensive testing have shown that for the present purpose surface sections as large as Mo_7O_{30} are sufficient to accurately represent local electronic properties of the surface [22-24]. In addition, the Mo_7O_{30} section is augmented by saturating dangling oxygen bonds at its periphery with hydrogen to yield the embedded surface cluster $\text{Mo}_7\text{O}_{30}\text{H}_{18}$ sketched in Fig. 1b. Terminating hydrogen atoms are placed near peripheral oxygen at O-H distances of 0.97 Å each, in accordance with the recipe given by Hermann et al. [41, 23, 24] and described in detail in [42]. It is found that corresponding electronic structure data for this cluster are in very good agreement with those from a larger surface cluster, $\text{Mo}_{15}\text{O}_{56}\text{H}_{22}$, see Fig. 2a, which confirms the above statement concerning cluster size convergence. The $\text{Mo}_{15}\text{O}_{56}\text{H}_{22}$ surface cluster is also used to model oxygen vacancies at the $\text{MoO}_3(010)$ surface where oxygen is removed from one of the three differently coordinated surface sites O(1-3) and the resulting vacancy cluster, $\text{Mo}_{15}\text{O}_{55}\text{H}_{22}$, is allowed to relax in response to the vacancy.

Electronic ground and core excited states of the above clusters are calculated using density functional theory (DFT) together with generalized gradient corrected exchange and correlation functionals according to Perdew, Burke, and Ernzerhof (RPBE) [25, 26]. The Kohn-Sham orbitals are represented by linear combinations of atomic orbitals (LCAO) using

extended basis sets of contracted Gaussians. For the ground state calculations and geometry optimizations oxygen and hydrogen are represented by all-electron DZVP basis sets ([4s4p] and [2s], respectively) while molybdenum is described using an effective core potential (ECP) together with a valence basis set [6s5p4d] for the 14 outermost electrons. For the evaluation of the X-ray absorption spectra the basis set at the excited oxygen center is chosen to be IGLO-III type ([7s6p2d]) [27] in order to adequately describe inner shell relaxation effects while the other oxygen centers in the cluster are accounted for by ECPs for the 1s shell and [3s3p1d] valence basis sets to avoid 1s core orbital mixing [28]. This approximation is found to result in faster convergence of the electronic structure compared to an all-electron treatment while introducing only negligible effects on the computed excitation spectra [29]. For all calculations the local basis set code StoBe [30] is employed.

The calculations of O 1s X-ray absorption spectra for the surface clusters are performed within Slater's transition potential approach [31, 32] in combination with a double basis set technique [33, 34]. This approach implies the use of a half occupied O 1s core orbital at the ionization site, thereby accounting for partial relaxation due to the presence of the excited electron. It has been proven earlier that, within this approach, final state relaxation effects are taken care of up to second order in the energy achieving a balance between the two relaxation mechanisms, core and valence type, and to yield extremely accurate results in the case of XAS calculations of light atoms [35]. The computed orbital energies and corresponding dipole transition matrix elements (determining absorption intensities) are convoluted using Gaussian broadening of varying width to mimic instrumental, vibrational, and life-time broadening. A full-width-at-half-maximum (fwhm) value of 0.5 eV is applied below ionization threshold while within 10 eV above threshold the broadening is increased linearly to 4.5 eV and kept fixed at this value for higher energies. For further details see also Refs. [7, 36]. In Slater's transition potential approach the electronic core hole relaxation of the ionized final state is not fully accounted for. This incomplete relaxation can be corrected in an approximate way by shifting all excitation energies by the difference of the ionization potential evaluated with the transition potential method and the corresponding value from Δ Kohn-Sham (Δ SCF) calculations, resulting in a global downward shift of ca. 2 eV. Further, relativistic corrections can be accounted for by an additional upward shift of the computed spectra by 0.33 eV [37].

The calculation of theoretical NEXAFS spectra in the present work is based on core to unoccupied orbital excitations that are determined by dipole transitions. Hence, angle-resolved spectral intensities $I(E, \vartheta, \varphi)$ are determined by corresponding dipole transition matrix elements \underline{m} together with angle dependent factors involving the polarization vector \underline{e} of the incoming radiation where

$$\begin{aligned} I(E, \vartheta, \varphi) &= \chi \cdot E \cdot (\underline{m} \cdot \underline{e})^2 = \chi \cdot E \cdot (m_x e_x + m_y e_y + m_z e_z)^2 \\ &= \chi \cdot E \cdot [\sin^2 \vartheta (m_x \cos \varphi + m_y \sin \varphi)^2 + \cos^2 \vartheta m_z^2 \\ &\quad + 2 \sin \vartheta \cos \vartheta (m_x \cos \varphi + m_y \sin \varphi) m_z] \quad . \end{aligned} \quad (1)$$

Here χ is a global scaling factor and E denotes the transition energy while ϑ, φ are polar and azimuthal angles of the photon polarization vector defined by

$$\underline{e} = (e_x, e_y, e_z) = (\sin \vartheta \cos \varphi, \sin \vartheta \sin \varphi, \cos \vartheta) \quad . \quad (2)$$

The transition dipole matrix elements \underline{m} involve the initial core orbital φ_i and final excited state orbitals φ_f where

$$\underline{m} = (m_x, m_y, m_z) = \langle \varphi_f | \mathbf{q} \cdot \mathbf{r} | \varphi_i \rangle \quad . \quad (3)$$

According to (1) the angle integrated intensity $I(E)$ is given by

$$I(E) = \int I(E, \vartheta, \varphi) d\Omega = 4\pi/3 \cdot \chi \cdot E \cdot (m_x^2 + m_y^2 + m_z^2) \quad (4)$$

If the theoretical angle-resolved core excitation spectra are to be compared with measured NEXAFS spectra the experimental conditions concerning angle dependence have to be taken into account. In the present measurements, see below, the MoO_3 samples exhibit some degree of rotational disorder likely due to the interaction of the oxide with the hexagonal Au(111) substrate. This effect can be simulated in the calculations by averaging the theoretical spectral intensities (1) over the azimuthal angle φ of the photon polarization vector which leads to

$$I(E, \vartheta) = \chi \cdot E \cdot [\frac{1}{2} (m_x^2 + m_y^2) \sin^2 \vartheta + m_z^2 \cos^2 \vartheta] \quad (5a)$$

or

$$I(E, \Theta) = \chi \cdot E \cdot [\frac{1}{2} (m_x^2 + m_y^2) \cos^2 \Theta + m_z^2 \sin^2 \Theta] \quad (5b)$$

where $\Theta = 90 - \vartheta$ is the angle of the photon beam with respect to the surface normal direction. Equation (5b) is used to calculate all theoretical angle-resolved NEXAFS spectra presented in this work.

3. Experimental Details

NEXAFS spectra of the $\text{MoO}_3(010)$ surface were recorded in total yield detection at the undulator beam line UE52-PGM of the Berlin synchrotron facility BESSY. The sample was prepared by first evaporating Mo at room temperature on Au(111) substrate under ultra high vacuum conditions. Then the sample was transferred in a high-pressure cell directly connected to the main chamber by a gate valve where the sample was heated for 10 minutes at 400°C in 50 mbar O_2 . The continuous O_2 flow was applied in order to minimize contaminations. LEED patterns of the sample show that the in-plane (100) and (001) directions exhibit rotational disorder with some preferential azimuthal orientations, likely due the weak interaction of the oxide with the hexagonal Au(111) substrate. Further details of the experimental setup are given in ref. [38].

4. Results and Discussion

4.1. Clean $\text{MoO}_3(010)$ Surface

In Fig. 3a we compare angle-resolved O 1s core excitation spectra calculated for the present surface clusters with corresponding experimental NEXAFS data for the clean $\text{MoO}_3(010)$ surface. The measurements refer to two different polarization directions, normal ($\Theta = 0^\circ$) and near-grazing ($\Theta = 70^\circ$) incidence of the photon beam. For normal incidence the agreement between theory and experiment is very good, particularly in the energy region up to ionization threshold, 536 eV, which exhibits the most prominent spectral features. Above the ionization threshold theoretical and experimental data seem to refer to different broadening but the spectra remain in qualitative agreement. For near-grazing incidence of the photon beam, $\Theta = 70^\circ$, the agreement between theory and experiment is less obvious. The discrepancy may be explained by corrections in the experimental polar angle Θ due to Fresnel

diffraction effects at the surface which result in an effective angle of incidence differing from that determined by macroscopic beam adjustment. This is suggestive from a comparison of the theoretical spectrum for $\Theta = 50^\circ$ with the experiment for $\Theta = 70^\circ$ in Fig. 3a which yields rather good agreement. Possible unevenness of the surface could also influence the effective angle of incidence of the X-ray beam locally and could, thus, contribute to the discrepancy between theoretical and experimental spectra near grazing incidence.

Fig. 3b shows a decomposition of the theoretical angle-resolved NEXAFS spectra into individual contributions from the three non-equivalent oxygen sites, O(1-3) for photon incidence angles $\Theta = 0^\circ, 50^\circ, 70^\circ$. For normal incidence ($\Theta = 0^\circ$) the intensities of the theoretical spectra are determined by in-plane matrix elements, m_x and m_y , in equation (5b). Thus, according to (3) electronic transitions involving final state orbitals containing O $2p_x$ and $2p_y$ character will mainly contribute to the spectral intensities. In contrast, at near grazing incidence ($\Theta = 70^\circ$) spectral intensities are determined mainly by matrix elements normal to the crystal surface, m_z , and transitions involving final state orbitals with O p_z character dominate the spectrum. This connection between angular behavior and character of final state orbitals can be used for a detailed interpretation of the experimental NEXAFS spectra and allows discrimination between differently coordinated oxygen.

The theoretical spectra for core excitation at O(1) and O(2) are, in the energy region between 530 and 533 eV, both dominated by two peaks which arise from O 1s core excitation to unoccupied orbitals with antibonding O2p - Mo4d character as shown by a detailed analyses of the final state orbitals. In both cases the peak at lower energy refers to orbitals where the O 2p admixture points perpendicular to the corresponding O - Mo bond whereas the peak at higher energy is due to orbitals with O 2p admixture pointing along the O - Mo bond. Obviously, the different amount of antibonding character of the two types of orbitals explains the energetic peak sequence. In addition, the symmetry of the O 2p admixture can describe the angle dependence of the corresponding peaks.

For core excitations at the molybdenyl site O(1), see Fig. 1, the low-energy peak is attributed to final state orbitals described by O2p_x - Mo4d_{xz} and O2p_y - Mo4d_{yz} mixtures, labeled A1, A1' and visualized in Fig. 4a. Therefore, corresponding dipole matrix elements m_x, m_y dominate in (5b) and the NEXAFS peak assumes maximum intensity at normal

incidence of the photon beam while its intensity becomes smallest at grazing incidence. In contrast, the high-energy peak originates from excitations to final state orbitals of $O2p_z - Mo4d_z^2$ and $O2p_z - Mo4d_{x^2-y^2}$ character, labeled B1, B1', see Fig. 4a. As a result, dipole matrix elements m_z , dominate in (5b) and the NEXAFS peak grows in intensity from normal to grazing incidence of the photon beam. Core excitations at the asymmetric bridging site O(2), see Fig. 1, follow the same scheme as described for O(1) except that the O - Mo bond at the excitation site points almost parallel to the surface rather than perpendicular. Here the low-energy peak is assigned to final state orbitals described by $O2p_x - Mo4d_{xy}$ and $O2p_z - Mo4d_{yz}$ mixtures, labeled A2, A2' and visualized in Fig. 4b. Thus, dipole matrix elements m_x and m_z contribute in (5b) and the intensity of the NEXAFS peak is only weakly dependent on the angle of incidence of the photon beam. This is found also for the high-energy peak which originates from excitations to final state orbitals of mixed $O2p_y -$ and $O2p_z - Mo4d_{yz}$ character, labeled B2, see Fig. 4b. Core excitations at the symmetric bridging site O(3), see Fig. 1, can be characterized completely analogous to those at O(1) and O(2) resulting, however, in a somewhat more complex angle dependence of the corresponding NEXAFS peaks due to the more intricate coordination environment at O(3). Altogether, the theoretical spectra for core excitation at the three differently coordinated oxygen sites show pronounced differences in their dependence on photon incidence angle in the energy region between 530 and 533 eV. This can be used to discriminate between the O(1), O(2), and O(3) species in experimental angle-resolved NEXAFS spectra for the $MoO_3(010)$ surface.

4.2. Oxygen deficient $MoO_3(010)$ Surface

Here we focus on oxygen vacancies at the $MoO_3(010)$ surface that appear when oxygen is removed from both the terminal O(1) and the asymmetrical bridging O(2) sites. Previous DFT cluster studies [4, 39] have shown that the removal of oxygen from these sites is energetically expensive but more favorable compared with the O(3) site. Further, geometric relaxation near the vacancy sites is rather local and leads, for O(1) and O(2) vacancies, to the same final vacancy geometry, see Fig. 2b. In this geometry a singly coordinated oxygen, $O(1)^*$, originating from the complementary site to where the oxygen was removed, O(1) or O(2), stabilizes in the intermediate region between the two sites forming a bond which is comparable in strength to the initial O(1)-Mo bond (with the same bond length d_{nn} , see Table

1) at an angle of about 45° with respect to the (010) surface, see Fig. 2b. These findings have been confirmed by the present geometry optimizations on a vacancy cluster $\text{Mo}_{15}\text{O}_{55}\text{H}_{22}$ allowing all atoms, except peripheral oxygen and hydrogen, to relax in response to the oxygen removal.

Due to the similarity in the local binding environment, core excitations originating at the $\text{O}(1)^*$ center of the oxygen deficient surface are found to involve very similar final state orbitals, antibonding $\text{O}2p$ - $\text{Mo}4d$ mixtures of different symmetry. This results in a two-peak structure of the excitation spectrum below ionization threshold in close correspondence with that discussed earlier for the $\text{O}(1)$ and $\text{O}(2)$ centers of the clean MoO_3 surface. However, the tilted orientation of the $\text{O}(1)^*$ -Mo bond compared with $\text{O}(1)$ -Mo, $\text{O}(2)$ -Mo leads to a different angle dependence of the excitation spectrum. This is obvious from a comparison of the different spectra in Fig. 5. The dependence of the $\text{O}(1)^*$ derived spectra on the photon incidence angle is rather different and less pronounced compared with those for $\text{O}(1)$, $\text{O}(2)$ which can be explained by the relative importance of the corresponding dipole transition matrix elements. Thus, angle dependent core excitation spectra may also be used to identify $\text{O}(1)^*$ species at the oxygen deficient $\text{MoO}_3(010)$ surface when experimental angle-resolved NEXAFS spectra become available.

The existence of a strongly tilted $\text{O}(1)^*$ species has been discussed controversially in the literature. Recent periodic DFT+U studies [42] seem to suggest that for an $\text{O}(1)$ vacancy at the $\text{MoO}_3(010)$ surface the nearby $\text{O}(1)^*$ species remains close to its initial asymmetric bridging $\text{O}(2)$ site even after relaxation, in contrast to our findings of a tilted $\text{O}(1)^*$ species. This has been attributed to incomplete electron localization of the DFT approach but further work is needed to resolve this issue. Here a combined theoretical and experimental NEXAFS study can give the decisive answer.

5. Conclusions

The (010) surface of single crystal MoO_3 has been shown to provide a useful model of more complex molybdenum oxide based industrial catalysts since as it retains their variability and richness of oxygen sites in a well defined crystal structure. Here the present DFT cluster

studies on local sections of the $\text{MoO}_3(010)$ surface together with corresponding angle-resolved NEXAFS measurements yield a rather detailed picture of the electronic structure as well as oxygen core excitations at the surface. Differently coordinated oxygen species at the surface, which are believed to play an active role in catalytic oxidation reactions at molybdenum oxide based catalysts, are found to exhibit pronounced differences concerning calculated energetics, spectral shape, and photon incidence dependence of their core excitations. The sensitivity of the spectral intensities to the symmetry of corresponding final state orbitals is a key element that allows one to discriminate between oxygen of similar chemical environment but differing by the orientation in the crystal. This has been clearly demonstrated in this work for the three differently coordinated oxygen species of clean $\text{MoO}_3(010)$ but also for oxygen near vacancies at the oxygen deficient $\text{MoO}_3(010)$ surface. Thus, the theoretical information can be used to identify the oxygen species unambiguously in angle-resolved NEXAFS measurements providing experimentalists with atom scale information about binding and local coordination in catalytic systems. While $\text{MoO}_3(010)$ surface systems are excellent model systems to examine catalytic behavior under well-defined experimental conditions more realistic information may be obtained from studying catalytic MoO_3 nano-particles or thin MoO_3 layers on metal substrate like $\text{Au}(111)$ [40]. Theoretical studies along these lines are presently under way.

Acknowledgments

One of the authors, M. C., acknowledges financial support from the Alexander-von-Humboldt foundation. This work was partly supported by the Deutsche Forschungsgemeinschaft through its Sonderforschungsbereich 546, ‘Transition metal oxide aggregates’.

Tables

Table 1

O-Mo bond distances for singly, doubly, and triply coordinated oxygen, O(1), O(2), O(3), at the $\text{MoO}_3(010)$ surface, see Fig. 1. The distances d_{nn} , $d_{\text{nn}2}$, $d_{\text{nn}3}$ refer to first, second, and third nearest Mo neighbors, respectively. Oxygen vacancies at either O(1) or O(2) lead to the same singly-coordinated O(1)* species in their neighborhood at the surface, see text and Fig. 4. Their d_{nn} value is also included in the table. All distances are given in Angstrom units.

	d_{nn}	$d_{\text{nn}2}$	$d_{\text{nn}3}$
O(1)	1.67	---	---
O(2)	1.73	2.25	---
O(3)	1.94	1.94	2.33
O(1)*	1.67	---	---

References

- [1] R. C.N.R., and B. Raven, *Transition metal oxides*, VCH Publishers, NYC-Weinheim-Cambridge, 1995.
- [2] B. Grzybowska, A. Mazurkiewicz, and J. Sloczynski, *App. Cat.*, **13** (1985) 223.
- [3] L.E. Cadus, M.C. Abello, M.F. Gomez, and J.B. Rivarola, *Ind. and Eng. Chem. Res.*, **35** (1996) 14.
- [4] K. Hermann, and M. Witko, in *Oxide Surfaces*, edited by D.P. Woodruff (Elsevier, NYC, 2001), p. 136.
- [5] E.R. Braithwaite, and J. Haber, *Molybdenum: An outline of its chemistry and uses*, Elsevier Science, Amsterdam, 2001.
- [6] K. Hermann, M. Witko, R. Druzinic, A. Chakrabarti, B. Tepper, M. Elsner, A. Gorschlüter, H. Kuhlenbeck, and H.-J. Freund, *J. Electron Spectrosc. Relat. Phenom.*, **99** (1999) 245.
- [7] C. Kolczewski, and K. Hermann, *J. Chem. Phys.*, **118** (2003) 7599.
- [8] C. Kolczewski, R. Püttner, M. Martins, A.S. Schlachter, G. Snell, M.M. Sant'Anna, K. Hermann, and G. Kaindl, *J. Chem. Phys.*, **124** (2006) 034302.
- [9] C. Kolczewski, R. Püttner, O. Plashkevych, H. Ågren, V. Staemmler, M. Martins, G. Snell, A.S. Schlachter, M. Sant'Anna, G. Kaindl, and L.G.M. Pettersson, *J. Chem. Phys.*, **115** (2001) 6426.
- [10] M. Nyberg, M. Odelius, A. Nilsson, and L.G.M. Pettersson, *J. Chem. Phys.*, **119** (2003) 12577.
- [11] C. Kolczewski, F.J. Williams, R.L. Cropley, O.P.H. Vaughan, A.J. Urquhart, M.S. Tikhov, R.M. Lambert, and K. Hermann, *J. Chem. Phys.*, **125** (2006) 034701.
- [12] F.J. Williams, R.L. Cropley, O.P.H. Vaughan, A.J. Urquhart, M.S. Tikhov, C. Kolczewski, K. Hermann, and R.M. Lambert, *J. Am. Chem. Soc.*, **127** (2005) 17007.
- [13] M. Cavalleri, L.Å. Näslund, D.C. Edwards, P. Wernet, H. Ogasawara, S. Myneni, L. Ojamäe, M. Odelius, A. Nilsson, and L.G.M. Pettersson, *J. Chem. Phys.*, **124** (2006) 194508.
- [14] M. Cavalleri, H. Ogasawara, L.G.M. Pettersson, and A. Nilsson, *Chem. Phys. Lett.*, **364** (2002) 363.
- [15] C. Kolczewski, and K. Hermann, *Theo. Chem. Acc.*, **114** (2005) 60.
- [16] Ph. Wernet, D. Nordlund, U. Bergmann, M. Cavalleri, M. Odelius, H. Ogasawara, L.Å. Näslund, T.K. Hirsch, L. Ojamäe, P. Glatzel, L.G.M. Pettersson, and A. Nilsson, *Science*, **304** (2004) 995.
- [17] K.R. Wilson, M. Cavalleri, B.S. Rude, R.D. Schaller, A. Nilsson, L.G.M. Pettersson, N. Goldman, T. Catalano, J.D. Bozek, and R.J. Saykally, *J. Phys. Cond. Mat.*, **14** (2002) L221.

- [18] M.A. Banares, and J.L.G. Fierro, *Catal. Lett.*, **17** (1993) 205.
- [19] M.A. Banares, J.L.G. Fierro, and J.B. Moffat, *J. Catal.*, **142** (1993) 406.
- [20] M.A. Banares, I. Rodriguez-Ramos, A. Guerrero-Ruiz, J.L.G. Fierro, B.R. Hodnett, A. Parmaliana, K. Klier, U.S. Ozkan, O.V. Krylov, J.B. Moffat, C. Li, and I.E. Wachs, *Stud. Surf. Sci. Catal.*, **75** (1993) 1131.
- [21] L. Kihlberg, *Acta Chem. Scandinava*, **17** (1963) 1485.
- [22] K. Hermann, A. Michalak, and M. Witko, *Catal. Today*, **32** (1996) 321.
- [23] K. Hermann, M. Witko, and A. Michalak, *Catal. Today*, **50** (1999) 567.
- [24] A. Michalak, K. Hermann, and M. Witko, *Surf. Sci.*, **366** (1996) 323.
- [25] B. Hammer, L.B. Hansen, and J.K. Norskov, *Phys. Rev. B*, **59** (1999) 7413.
- [26] J.P. Perdew, K. Burke, and M. Ernzerhof, *Phys. Rev. Lett.*, **77** (1996) 3865.
- [27] W. Kutzelnigg, U. Fleischer, and M. Schindler, *NMR-Basic Principles and Progress*, Springer-Verlag, Heidelberg, 1990.
- [28] L.G.M. Pettersson, U. Wahlgren, and O. Gropen, *Chem. Phys.*, **80** (1983) 7.
- [29] M. Nyberg, *Ph.D. Thesis*, Stockholm University, 2000.
- [30] K. Hermann, L.G.M. Pettersson, M.E. Casida, C. Daul, A. Goursot, A. Koester, E. Proynov, A. St-Amant, D.R. Salahub, V. Carravetta, H. Duarte, C. Friedrich, N. Godbout, J. Guan, C. Jamorski, M. Leboeuf, M. Leetmaa, M. Nyberg, L. Pedocchi, F. Sim, L. Triguero, and A. Vela, *StoBe software* (2005).
- [31] J.C. Slater, *Adv. Quant. Chem.*, **6** (1972) 1.
- [32] J.C. Slater, and K.H. Johnson, *Phys. Rev. B*, **5** (1972) 844.
- [33] L. Triguero, L.G.M. Pettersson, and H. Ågren, *J. Phys. Chem. A*, **102** (1998) 10599.
- [34] L. Triguero, L.G.M. Pettersson, and H. Ågren, *Phys. Rev. B*, **58** (1998) 8097.
- [35] M. Cavalleri, M. Odelius, D. Nordlund, A. Nilsson, and L.G.M. Pettersson, *Phys. Chem. Chem. Phys.*, **7** (2005) 2854.
- [36] C. Kolczewski, and K. Hermann, *Surf. Sci.*, **552** (2004) 98.
- [37] O. Takahashi, and L.G.M. Pettersson, *J. Chem. Phys.*, **121** (2004) 10339.
- [38] S. Guimond, Y. Romanysyn, H. Kuhlenbeck, and H.-J. Freund, *BESSY Ann. Rep.*, (2005).
- [39] R. Tokarz-Sobieraj, K. Hermann, and M. Witko, unpublished.
- [40] S.Y. Quek, M.M. Biener, J. Biener, C.M. Friend, and E. Kaxiras, *Surf. Sci.*, **577** (2005) L71.
- [41] K. Hermann and P.S. Bagus, *Phys. Rev.*, B20 (1979) 1603.
- [42] R. Coquet and D.J. Willock, *Phys. Chem. Chem. Phys.*, **7** (2005) 3819.

Figure captions

- Fig. 1. (a) Crystal structure of orthorhombic MoO_3 given by two adjacent bilayer sections along the (010) direction. Large balls refer to molybdenum centers while smaller balls denote oxygen. The view refers to the [100] direction where atom centers of the Mo_7O_{30} surface cluster are emphasized by shading. (b) Geometric structure of the embedded surface cluster $\text{Mo}_7\text{O}_{30}\text{H}_{18}$ used in the calculations. Non-equivalent oxygen centers, O(1-3) are labeled accordingly.
- Fig. 2. (a) Geometric structure of the embedded surface cluster $\text{Mo}_{15}\text{O}_{56}\text{H}_{22}$ used in the calculations for the clean MoO_3 surface. Non-equivalent oxygen centers, O(1-3) are labeled accordingly. (b) Relaxed geometry of the embedded surface cluster $\text{Mo}_{15}\text{O}_{55}\text{H}_{22}$ modeling oxygen vacancies at either the O(1) or O(2) site, see text. The oxygen $\text{O}(1)^*$ near the vacancy occupies a intermediate position between that of O(1) and O(2) at the clean MoO_3 surface, see Fig. 2a. The two vacancy sites are sketched by black dots.
- Fig. 3. (a) Comparison of theoretical (solid lines) and experimental (dotted lines) angle-resolved O 1s NEXAFS spectra of $\text{MoO}_3(010)$ as a function of the photon incidence angle Θ , see text. (b) Decomposition of the theoretical NEXAFS spectra into contributions from the three differently coordinated oxygen sites, O(1-3) for photon incidence angles $\Theta = 0^\circ, 50^\circ$, and 70° . The light gray vertical line indicates the position of the computed ionization potentials.
- Fig. 4. Theoretical angle-resolved O 1s NEXAFS spectra at (a) the terminal O(1) and (b) the asymmetric bridging O(2) site for photon incidence angles Θ between 0° and 90° . Corresponding final state orbitals of dominant peaks, labeled $\text{A1}^{(\epsilon)}$, $\text{B1}^{(\epsilon)}$ for O(1) and $\text{A2}^{(\epsilon)}$, B2 for O(2), are visualized by iso-surfaces to the left.
- Fig. 5. Comparison of theoretical angle-resolved O 1s NEXAFS spectra at O(1) and O(2) sites of the clean $\text{MoO}_3(010)$ surface with those of the $\text{O}(1)^*$ site near O(1) and O(2) vacancies at the defective surface, see Fig. 2 and text. The results are obtained from calculations using clusters $\text{Mo}_{15}\text{O}_{56}\text{H}_{22}$ and $\text{Mo}_{15}\text{O}_{55}\text{H}_{22}$, respectively.

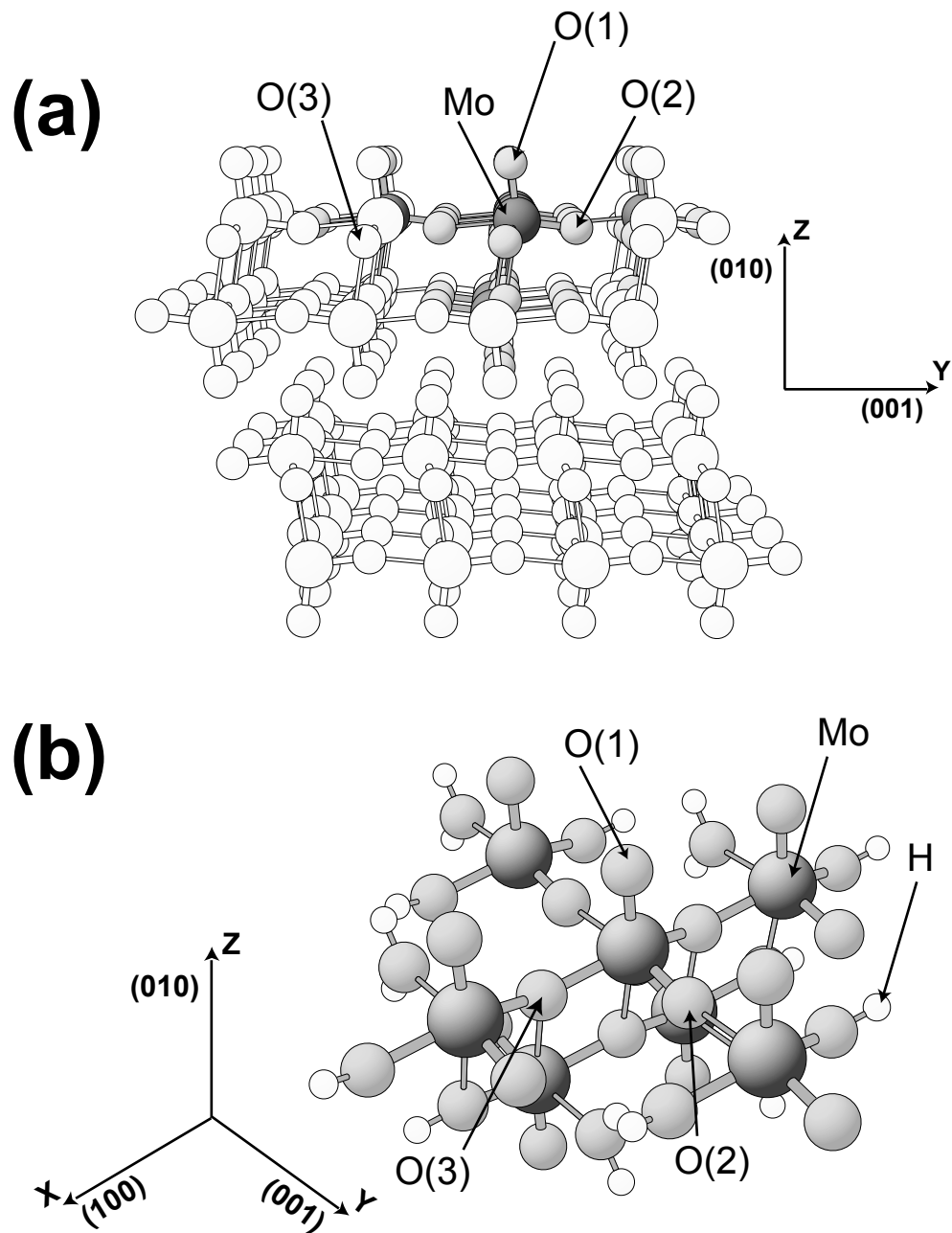
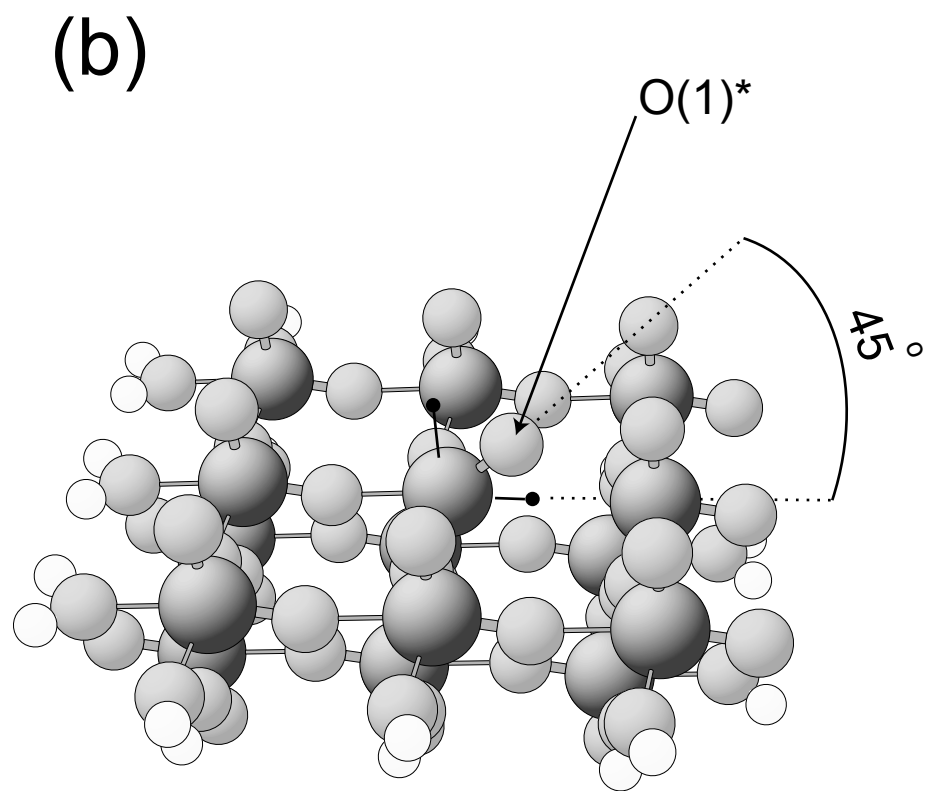
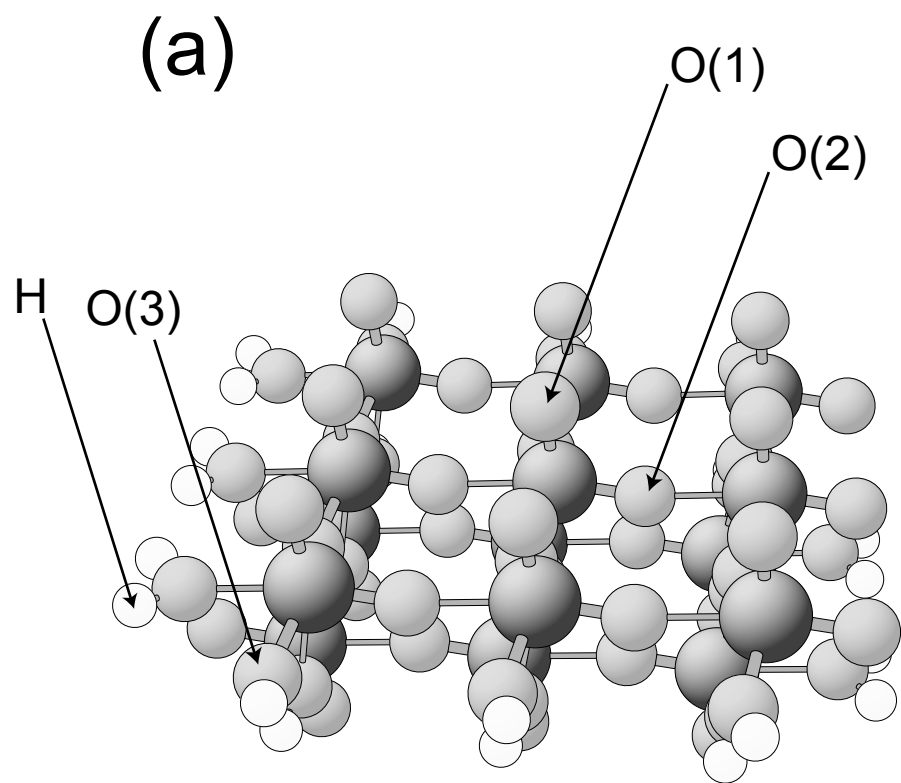


Figure 1, Cavalleri et al.



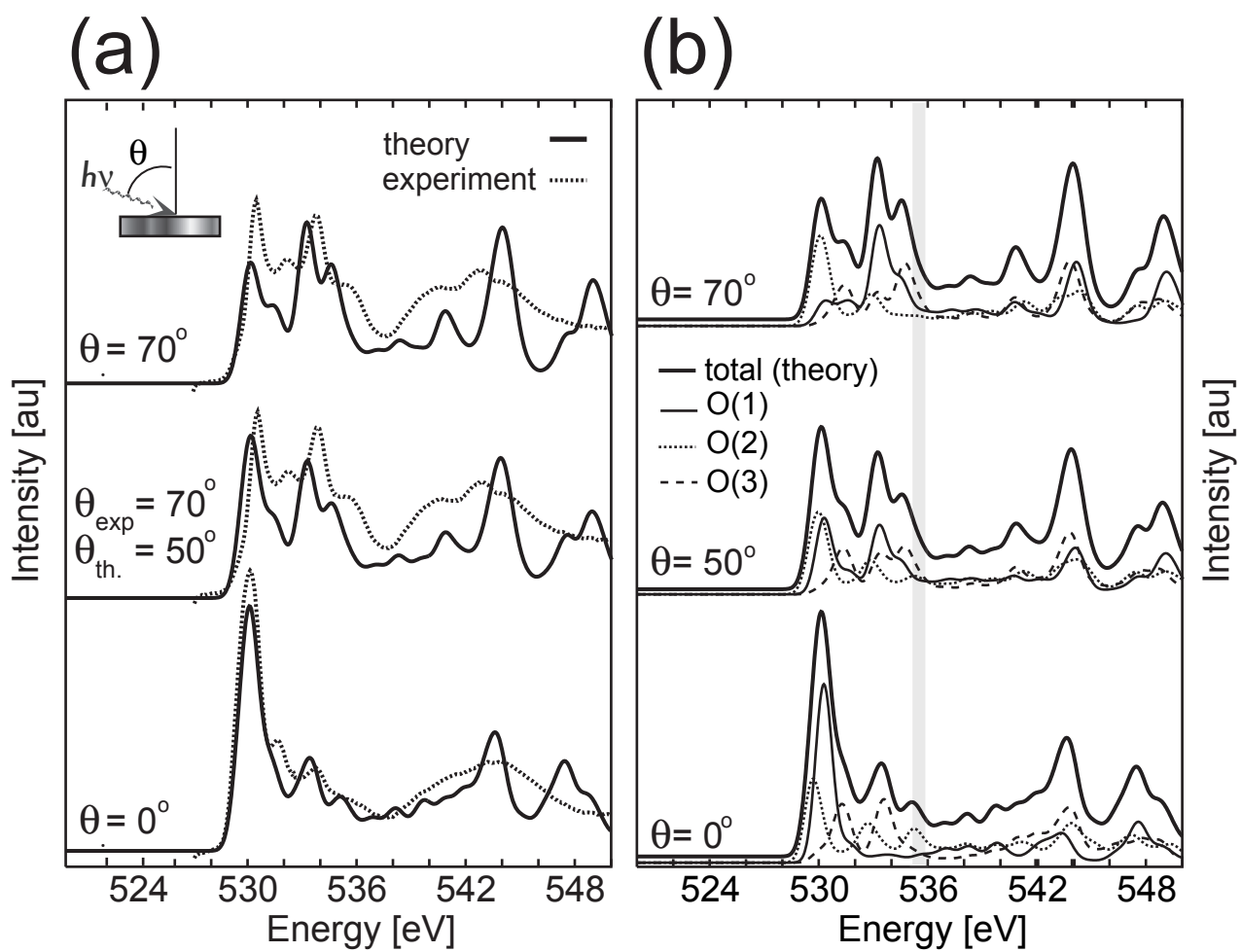
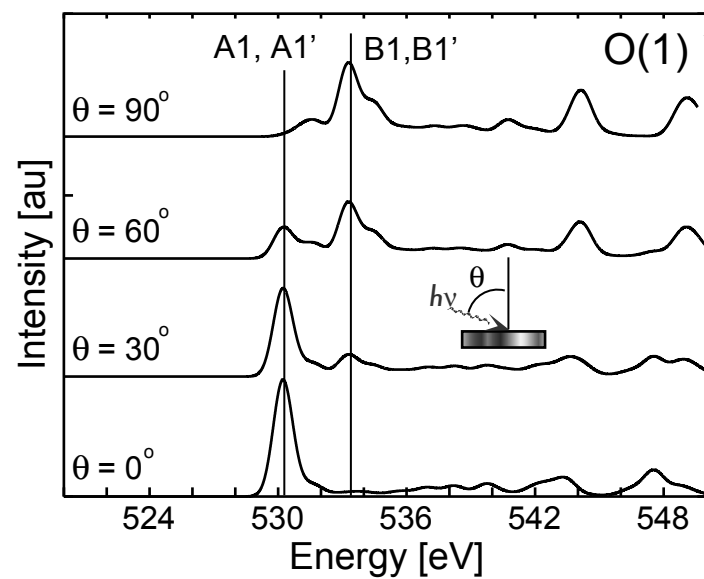


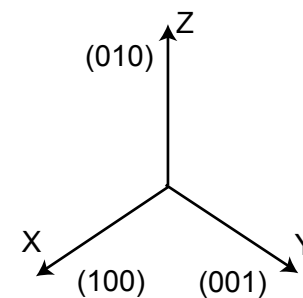
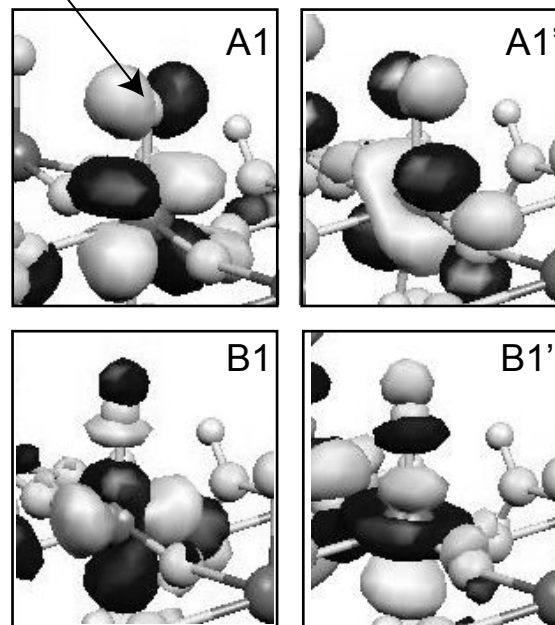
Figure 3, Cavalleri et al.

Figure 4, Cavalleri et al.

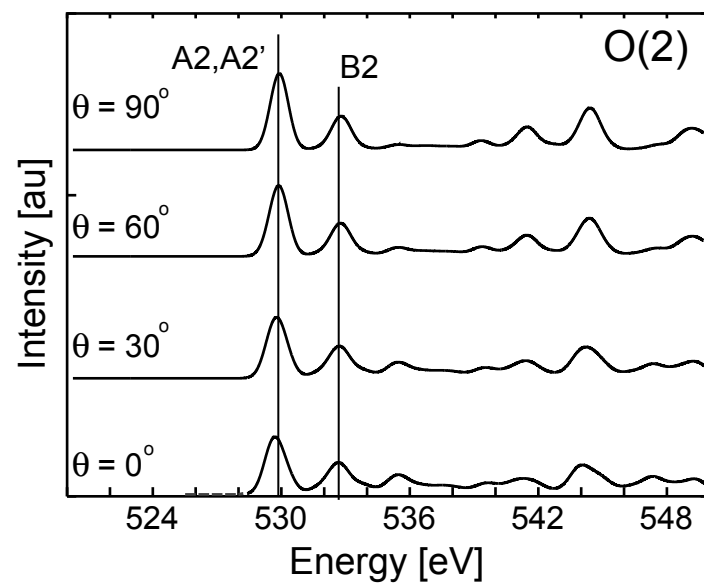
(a)



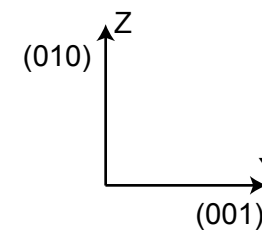
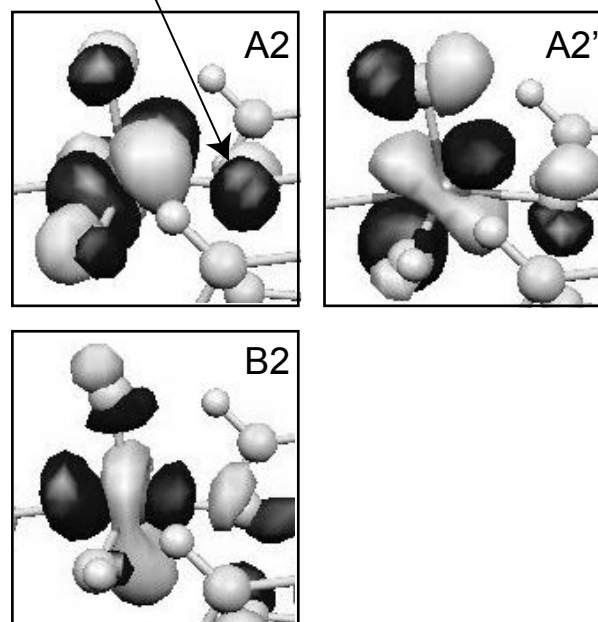
O(1)



(b)



O(2)



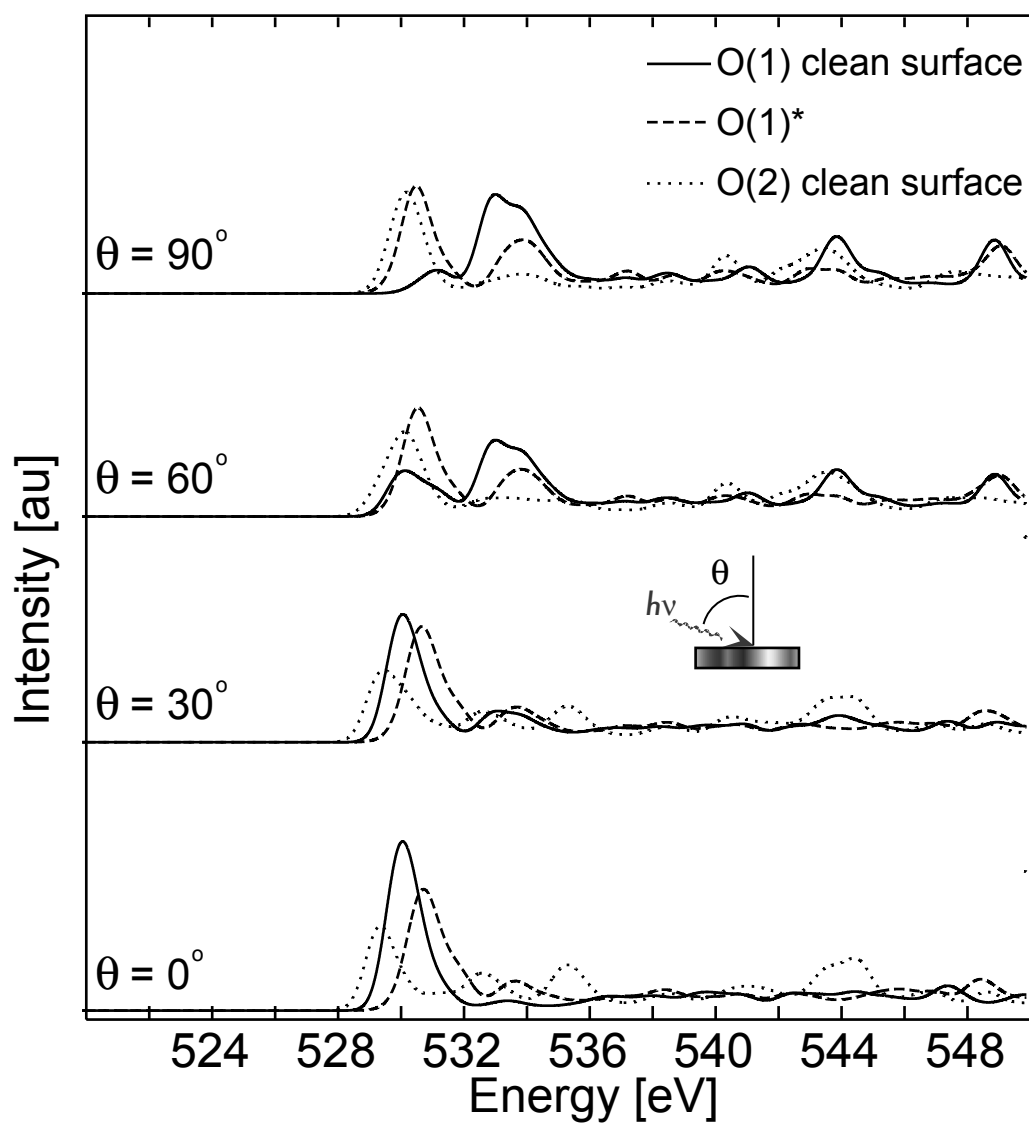


Figure 5, Cavalleri et al.